

This is a repository copy of *Tailored mesoscopic plasma accelerates electrons exploiting parametric instability*.

White Rose Research Online URL for this paper:

<https://eprints.whiterose.ac.uk/id/eprint/210856/>

Version: Published Version

---

**Article:**

Kumar, Rakesh Y., Sabui, Ratul, Gopal, R. et al. (9 more authors) (2024) Tailored mesoscopic plasma accelerates electrons exploiting parametric instability. *New Journal of Physics*. 033027. ISSN: 1367-2630

<https://doi.org/10.1088/1367-2630/ad2ffc>

---

**Reuse**

This article is distributed under the terms of the Creative Commons Attribution (CC BY) licence. This licence allows you to distribute, remix, tweak, and build upon the work, even commercially, as long as you credit the authors for the original work. More information and the full terms of the licence here:

<https://creativecommons.org/licenses/>

**Takedown**

If you consider content in White Rose Research Online to be in breach of UK law, please notify us by emailing [eprints@whiterose.ac.uk](mailto:eprints@whiterose.ac.uk) including the URL of the record and the reason for the withdrawal request.



PAPER • OPEN ACCESS

## Tailored mesoscopic plasma accelerates electrons exploiting parametric instability

To cite this article: Rakesh Y Kumar *et al* 2024 *New J. Phys.* **26** 033027

View the [article online](#) for updates and enhancements.

### You may also like

- [Identification and detection of high NO<sub>x</sub> emitting inland ships using multi-source shore-based monitoring data](#)  
Hongxun Huang, Chunhui Zhou, Changshi Xiao et al.
- [Efficient broadband sound absorption exploiting rainbow labyrinthine metamaterials](#)  
Fabio Nistri, Venus Hasanuzzaman Kamrul, Leonardo Bettini et al.
- [Dynamic control of the Bose-Einstein-like condensation transition in scalar active matter](#)  
Jonas Berx



## OPEN ACCESS

## RECEIVED

20 December 2023

## REVISED

29 February 2024

## ACCEPTED FOR PUBLICATION

4 March 2024

## PUBLISHED

18 March 2024

Original Content from  
this work may be used  
under the terms of the  
[Creative Commons  
Attribution 4.0 licence](#).

Any further distribution  
of this work must  
maintain attribution to  
the author(s) and the title  
of the work, journal  
citation and DOI.



## PAPER

## Tailored mesoscopic plasma accelerates electrons exploiting parametric instability

Rakesh Y Kumar<sup>1,2</sup> , Ratul Sabui<sup>1,2</sup> , R Gopal<sup>1</sup> , Feiyu Li<sup>3,8</sup> , Soubhik Sarkar<sup>1</sup> , William Trickey<sup>4</sup> ,  
M Anand<sup>1</sup> , John Pasley<sup>4</sup> , Z-M Sheng<sup>3,5</sup> , R M G M Trines<sup>6</sup> , R H H Scott<sup>6</sup> , A P L Robinson<sup>6</sup> ,  
V Sharma<sup>2</sup>  and M Krishnamurthy<sup>1,7,\*</sup> 

<sup>1</sup> Tata Institute of Fundamental Research, Hyderabad 500046, India<sup>2</sup> Indian Institute of Technology Hyderabad, Kandi 502285, India<sup>3</sup> SUPA, Department of Physics, University of Strathclyde, Glasgow G1 1XQ, United Kingdom<sup>4</sup> York Plasma Institute, Department of Physics, University of York, York YO10 5DD, United Kingdom<sup>5</sup> Laboratory for Laser Plasmas and School of Physics and Astronomy, Shanghai Jiao Tong University, Shanghai, People's Republic of China<sup>6</sup> Central Laser Facility, Rutherford Appleton Laboratory, Chilton, Didcot OX10 0QX, United Kingdom<sup>7</sup> Tata Institute of Fundamental Research, Mumbai 400005, India<sup>8</sup> Currently at New Mexico Consortium, Los Alamos, NM 87544, United States of America.

\* Author to whom any correspondence should be addressed.

E-mail: [mkrism@tifr.res.in](mailto:mkrism@tifr.res.in)**Keywords:** laser plasma particle acceleration, plasma physics, femtosecond lasers

## Abstract

Laser plasma electron acceleration from the interaction of an intense femtosecond laser pulse with an isolated microparticle surrounded by a low-density gas is studied here. Experiments presented here show that optimized plasma tailoring by introducing a pre-pulse boosts parametric instabilities to produce MeV electron energies and generates electron temperatures as large as 200 keV with the total charge being as high as 350 fC/shot/sr, even at a laser intensity of a few times  $10^{16}$  Wcm<sup>-2</sup>. Corroborated by particle-in-cell simulations, these measurements reveal that two plasmon decay in the vicinity of the microparticle is the main contributor to hot electron generation.

## 1. Introduction

High-intensity laser-plasma driven particle acceleration has been studied over the past few decades and a considerable progress/development [1–4] has been achieved. Various mechanisms and schemes responsible for energetic *hot* electrons were studied in detail including resonance absorption [5], collisionless absorption [6–9], laser wakefield acceleration [10–12], space-charge field effects in solids [13–17], surface plasma waves [14, 18, 19], direct laser acceleration [20–22], vacuum laser acceleration [23–25], etc to name a few. For electron acceleration in under dense plasmas where the electron density  $n_e \leq n_{cr}$  ( $n_{cr} = 1.1 \times 10^{21}/\lambda^2$  in cm<sup>-3</sup>, is the critical electron density,  $\lambda$  is the wavelength of the incident laser pulse), from typically gas targets, the essential mechanism is to excite longitudinal plasma waves through ponderomotive acceleration by ultrashort (<100 fs) ultra-intense ( $\sim 10^{18}$  Wcm<sup>-2</sup>) laser pulses. Electrons experience the static electric field from those excited plasma waves and are accelerated to relativistic energies.

In over-dense plasmas,  $n_e \geq n_{cr}$ , the laser intensity, polarization, contrast and the related parameter of pre-plasma scale length govern which of the many mechanisms for electron acceleration are significant. A small fraction of the electrons are accelerated to very high energies and the temperature scaling of these electrons, as compiled from various experiments, calculations, and theories is approximated by  $T_e \sim m_e c^2 (\sqrt{1 + a_0^2/2} - 1)$  [26], where  $a_0$  is the normalized peak strength of the laser given by  $a_0 = \sqrt{I/I_0} \cdot \lambda^2$ , where  $I$ , the peak laser intensity in units of W cm<sup>-2</sup>,  $\lambda$  is the driving laser wavelength in  $\mu$ m,  $I_0 = 1.37 \times 10^{18}$ . In both the over-dense and under-dense cases, it is pertinent to note that the generation of relativistic electrons needs laser intensities of the order of  $a_0 > 1$ , i.e  $I > 2 \times 10^{18}$  W cm<sup>-2</sup> for 800 nm laser

pulses. Of contemporary importance is the generation of *supra thermal* electrons, beyond those predicted by the scaling relation, reflected in both theoretical and computational work [27–29].

In this work, we present experiments where the target is a substrate-free mass-limited solid target suspended in vacuum. This is actualised through a jet of individual microparticles ( $15\ \mu\text{m}$  in size) immersed in low-density gas, irradiated by an intense  $10^{16}\ \text{Wcm}^{-2}$  ultra-short (25 fs) laser pulse. The peripheral gas ionizes to a low-density plasma while the solid microparticle forms a highly localized over-dense plasma. The hot electron emission temperature, defined by a Boltzmann distribution of emitted electron/x-ray energy, as  $k_B T_e$  ( $k_B$  is the Boltzmann constant), is as large as 200 keV. The laser parameters (1–3 mJ, 1 kHz) are different from those of contemporary experiments that either use larger laser energy (Joule class) pulses of longer duration ( $\geq 100$  fs) or 10–100 fold larger intensities ( $\geq 10^{18}\ \text{Wcm}^{-2}$ ). We propose that the combination of low-density plasma background and high densities in the microparticles brings out two plasmon decay (TPD) parametric instability and is responsible for the hotter electron generation.

Parametric instabilities like Stimulated Raman Scattering (SRS), TPD, and Stimulated Brillouin Scattering [9, 30] have been studied over several decades to understand the laser energy absorption, asymmetric compression, pre-heating of the target material, etc. in the context of inertial confinement fusion research [31]. SRS instability is a wave-growing mechanism in the plasma where incident pump laser pulse, an electromagnetic (E-M) wave of frequency ( $\omega_0$ ) decays in the  $n_{cr}$  to  $n_{cr}/4$  electron density region of plasma into a daughter electron plasma wave (Langmuir wave) of frequency  $\omega_e$  and a scattered E-M wave ( $\omega_s$ ) of either stokes and anti-stokes modes [32]. The quiver motion of electrons in the pump E-M laser field generates transverse current density and the exponential growth rate of the electron density oscillations depends on the angle between scattered E-M and pump E-M waves. The scattered E-M wave interferes (or beats) with the incident pump E-M wave leading to enhanced density fluctuations resonantly driven by resulting pondermotive force. The enhanced plasma wave amplitude in turn scatters more of the E-M wave (dipole radiation from the enhanced current density in the electron density compression of plasma wave) and consequently spikes the resulting pondermotive force. This cycle of amplification in both E-M waves causes exponential growth of the Langmuir wave. The quanta of Langmuir wave oscillations are termed plasmons ( $\omega_e$ ) and satisfy the phase matching condition ( $\omega_s = \omega_0 - \omega_e$ ) and the dispersion relation.

The incident laser E-M wave ( $\omega_0$ ) also decays resonantly into two daughter Langmuir waves of frequencies  $\omega_{e1}$  and  $\omega_{e2}$  around  $n_{cr}/4$  layer. These two plasmons satisfy the phase matching condition ( $\omega_0 = \omega_{e1} + \omega_{e2}$ ). The longitudinal electric field of the Langmuir wave interferes (or beats) with the plane polarized pump laser field and assists the exponential wave growth until the saturation is obtained due to non-linear processes [33]. Hence, TPD is an absolute instability. Around  $n_{cr}/4$  layer, the scattered E-M wave ( $\omega_s$ ) from SRS process phase matches and couples resonantly with pump laser ( $\omega_0$ ) to generate  $3\omega_0/2$  photons analogous to sum frequency generation and three-wave mixing process [34–36]. The production of  $3\omega_0/2$  harmonic radiation is a signature of TPD instability and is considered as a potential pre-plasma diagnostic to estimate cold plasma temperature around  $n_{cr}/4$  layer by analyzing the spectral splitting in the emitted radiation, intensity threshold for TPD, electrostatic wave scattering angle, origin of  $3\omega_0/2$  photons, turning point of the laser photons, etc. In most of the experimental geometries, the Langmuir wave K-vector is not parallel to the pump laser K-vector.

Non-linear parametric excitations (resonant and non-resonant) of plasma waves in a strongly inhomogeneous plasmas ( $L/\lambda \leq 10$ , even  $L/\lambda \leq 1$ ) differs significantly when compared to those in weakly inhomogeneous plasmas ( $L/\lambda \gg 10$ ),  $L$  is the plasma scale length and  $\lambda$  is the wavelength of the laser [37]. The former are produced using intense short-pulse ( $< 100$  fs) lasers, and the latter using long-pulse ( $> 1$  psec and nsec) lasers. The resonant unsaturated model [38] formulated for long pulse and weakly inhomogeneous plasmas, neglecting Langmuir wave decay instability for short laser pulses, estimates the growth of plasma wave amplitude. It is seen to depend on both laser (intensity,  $I_0$ , pulse width, pulse contrast, etc) and plasma properties (pre-plasma scale length, plasma temperature, the morphology of the pre-plasma, etc). In steeper electron density plasmas, the excitation of the instability is spatially confined, and the phase and frequency matching condition could be satisfied locally by plasmons with real frequencies. Two daughter plasmon waves in the TPD instability being electrostatic, undergo further damping and wave breaking, and cause enhanced absorption [39] leading to energetic (suprathermal) electron emission [40]. Usually, the component of SRS instability in the plasma wave growth process in comparison to the TPD is negligible.

The interaction of short ( $\simeq 100$  fs) laser pulses at moderate laser intensities ( $\simeq 10^{17}\ \text{Wcm}^{-2}$ ) with steep-density plasmas is scarcely studied. Veisz *et al* report detailed measurements of the  $3\omega_0/2$  harmonic radiation produced upon the interaction of a 100 fs,  $10^{17}\ \text{W cm}^{-2}$  intense laser with a polished Aluminium target [41]. A relatively strong inhomogeneous pre-plasma of  $L = 10\ \mu\text{m}$  scale length was produced using a pre-pulse traveling 12.5 nsec ahead of the main pulse. The  $\beta$  parameter for the direct coupling of  $\omega_0/2$  plasmon with laser photon was calculated and it is understood that for  $\lambda = 0.8\ \mu\text{m}$ ,  $T_e = 1\ \text{keV}$  and  $I_0 = 10^{16}$ – $10^{17}\ \text{W cm}^{-2}$ , direct coupling is possible. Furthermore, the pump laser intensity and scale length

dependent angular distribution of  $3\omega_0/2$  radiation were measured in the plasmas with range  $L = 0.8 - 7\mu\text{m}$  in the mild intensity regime ( $10^{16} - 10^{18} \text{ W cm}^{-2}$ ). It was experimentally proved that the observation of  $3\omega_0/2$  radiation with an increased bandwidth is a valuable pre-plasma diagnostic [42] to study the plasma temperature and growth rates of the plasma wave.

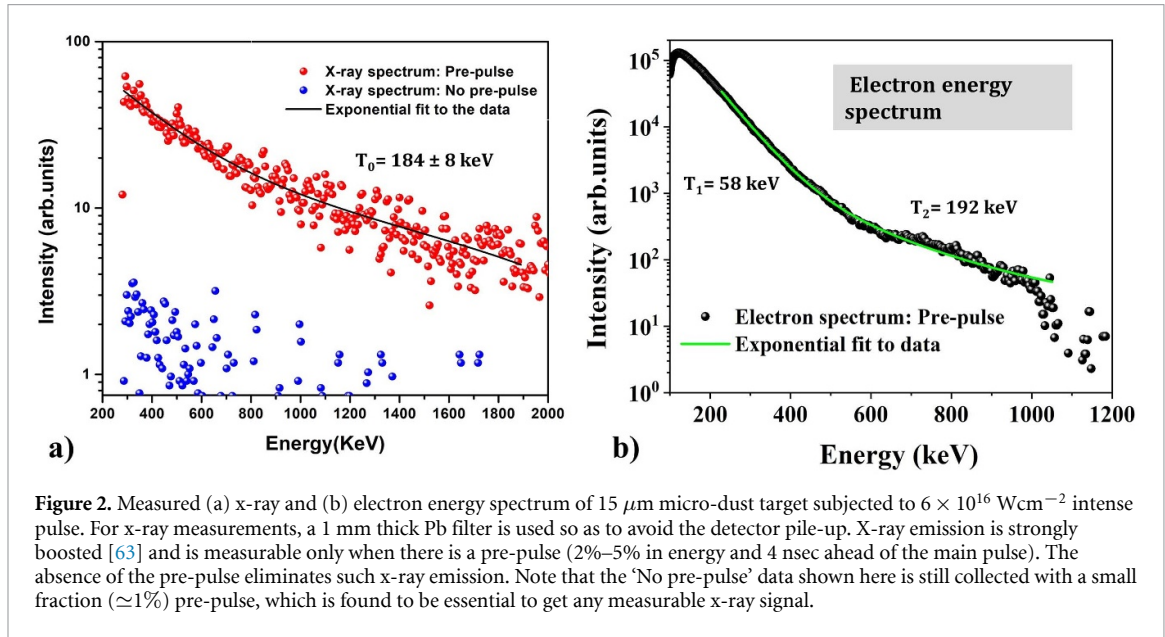
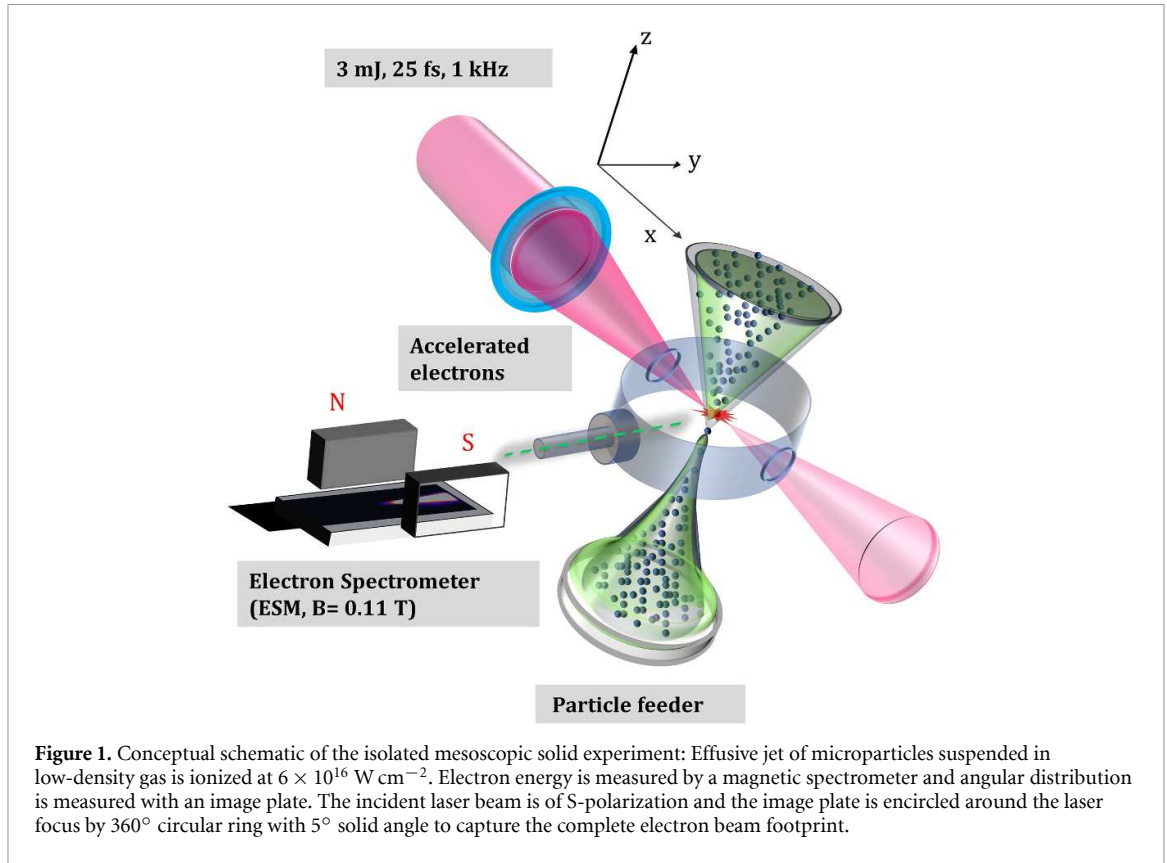
The intensity threshold ( $I_{th}$ ) was worked out analytically for nsec lasers interacting with weakly inhomogeneous plasmas, which is  $I_{th} \sim 2 \times 10^{16} T_e(\text{keV}) (\lambda_{\mu\text{m}} L_{\mu\text{m}}) \text{ W cm}^{-2}$  [32]. The inverse proportionality of the  $I_{th}$  with  $\lambda_{\mu\text{m}}$  and  $L_{\mu\text{m}}$ , and direct proportionality with  $T_e(\text{keV})$  is valid quantitatively for short pulse ( $\leq 100$  fs) lasers interaction with strongly inhomogeneous plasmas. Prashant Singh *et al* studied the onset of TPD instability in strong inhomogeneous plasmas for a wide variety of laser parameters (energy, pulse duration, and pulse contrast) [43, 44]. The pre-plasma scale length was varied by changing the contrast ( $10^{-5} - 10^{-9}$ ) of the laser pulse and at different intensities (of the order  $10^{17} - 10^{19} \text{ W cm}^{-2}$ ) by changing the laser pulse energy (50–140 mJ) and pulse duration (30–100 fs). Experimental measurements supported by analytical modeling of the TPD yield, TPD appeared at much lower intensities at longer pulse lengths ( $\simeq 100$  fs) and pre-plasma scale length was varied by changing the pulse contrast by 4 orders of magnitude, the  $I_{th}$  for high contrast pulse is observed to be 2 orders of magnitude larger. The most significant finding in these experiments is that TPD yield decreases exponentially below 100 fs in this intensity range. For a fixed pulse duration of 30 fs and 120 fs, no measurable TPD signal was emitted below 140 mJ and 65 mJ respectively. Recent developments in the short pulse ( $\simeq 100$  fs) laser interaction with the steep density gradient plasmas ( $L \simeq \lambda$ ) also include the study by I. Tsymbalov *et al*, where the hybrid SRS-TPD instability in the intensity regime  $10^{17} - 10^{19} \text{ W cm}^{-2}$  was investigated. The role of plasma wave excitation, and laser energy absorption at quarter critical density was studied using pondermotive force analysis [45–47].

In this work, we present both experimental and simulation data where strong, TPD emission of large bandwidth (in comparison to that of the pump laser pulse) is observed for 30 fs, 3 mJ laser pulses interacting with mass limited targets, in the non-relativistic intensity regime  $\sim 10^{16} \text{ W cm}^{-2}$  and assists electron acceleration to MeV energies. In the presence of a pre-pulse, the main laser pulse interaction with an isolated, size-limited solid micro-particle surrounded by a low-density gas (termed as micro-dust target in this paper) differs from that of plasma studies with solid targets [48, 49], high-density gas targets [10, 11] or microparticles in discharge tubes [50, 51]. Here, a low-density plasma region where the plasma waves can be generated, grown, and driven to a localized critical density ( $n_{cr}$ ) surface provides very suitable conditions for very hot electron generation. Features like parametric instabilities [52] can lead to enhanced electron acceleration even at lower intensities compared to those in experiments with the regular gas [53, 54], clusters [55–57] or solids targets [58]. We show here that features like: low-electron density ( $n_e$ ), long scale-length ( $L$ ) plasma, size-limited solid-density particle, and tailored pre-plasma, where the  $n_{cr}$  layer shape features are tailored by a separate pre-pulse, produces beam-like electron emission up to MeV energies even at  $10^{16} \text{ W cm}^{-2}$ . The maximum electron energy up to 1 MeV and  $k_B T_e$  as large as 200 keV that are typical in laser experiments at a hundred times larger intensities are seen. Electrons are emitted as two symmetrical beams controlled by laser polarization. The hot electron generation depends not only on the interaction at about  $n_{cr}$  region but also on the dynamical structure of the pre-plasma and low-density plasma electron density profile.

## 2. Experiments

Figure 1 shows the experimental schematic, where a microparticle suspended in a low-density gaseous background is subjected to  $10^{16} \text{ W cm}^{-2}$  laser intensities. Gas ionization occurs a few mm ahead of the laser focus (even at  $10^{13} \text{ W cm}^{-2}$ ). An increase in the intensity towards the laser focus raises the degree of ionization and thereby the electron density [59] gradient in the background plasma of the mesoscopic solid target. But at the solid-density microparticle, the electron density is increased sharply and exceeds critical density.

Delivery of solid microparticles for laser-plasma studies is detailed elsewhere [60, 61]. In brief, pressurized gas (such as  $N_2$ ), is ‘bubbled’ through hydrogen borate ( $H_3BO_3$ )  $15 \mu\text{m}$  micro crystals, to form a jet of particles, encompassed in the gas of pressure 0.5 mbar. A 25 fs, 3 mJ pulses focused to  $14 \mu\text{m}$  (FWHM) generates an intensity of  $6 \times 10^{16} \text{ W cm}^{-2}$ . The focal spot measurement was performed using a 2f–2f imaging setup and the measured FWHM of  $14 \mu\text{m}$  was used to compute the focal peak intensity of  $6 \times 10^{16} \text{ W cm}^{-2}$ . About 4 nsec ahead of the main pulse a pre-pulse of 2%–5% main pulse intensity is introduced. A photo-diode is used to measure the transmitted laser pulse and a single-channel pulse height analyzer is used to gate a NaI(Tl) x-ray detector. Gating selects only those laser shots that have the microparticles at the laser focus and, x-ray and electron emission are studied with different parameters like main laser pulse intensity, pre-pulse intensity, etc. The direct electron emission spectrum is measured using a magnetic spectrometer [62]. Image plates encapsulated with Al foil, encircling the laser focus are used to measure the angular distribution of electrons with energy  $\geq 150$  keV.



### 3. Experimental results

A microparticle that is 20 times in size as the laser wavelength is expected to behave like a solid substrate and 2D-PIC (particle-in-cell simulations) confirm this expectation. But here, as shown in figure 2(a), the measured x-ray emission spectra differ from predictions made by scaling laws [26]. X-rays measured across a 1 mm thick Pb filter (x-ray cut off energy  $\approx 88 \text{ keV}$ ) which reduces detector pile-up (photon count is at most one for every ten laser pulses) show x-ray energy up to 2 MeV with electron temperature of  $\approx 184 \pm 8 \text{ keV}$ . Direct electron spectra (shown in figure 2(b)) emission collected over tens of thousands of laser shots with a magnetic spectrometer show electron energies that extend to 1.2 MeV. An exponential fit to the Maxwellian curve (black and green curves in figure 2) following the Levenberg Marquardt algorithm yields two temperatures,  $N(E)dE = N_1 \exp(-E/k_B T_{e1}) + N_2 \exp(-E/k_B T_{e2})$  with  $k_B T_{e1}$  &  $k_B T_{e2}$  are 58 keV and 192 keV



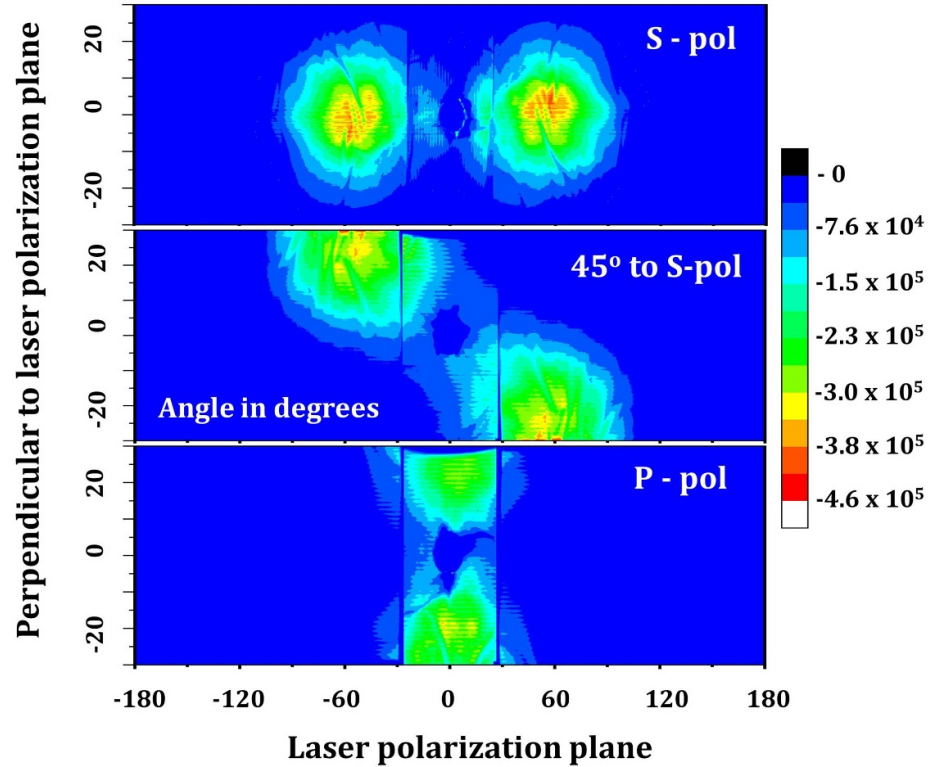


**Figure 3.** The rotation of the laser polarization rotates the electron beam emission in the laser polarization plane. Experimentally obtained electron angular distribution dependence on the laser polarization shows that the rotation of the electron beam by about  $45^\circ$  and  $90^\circ$  (p- polarization) to the laser polarization (S) plane. The vertical lines and discontinuity seen in the image are experimental artifacts. The horizontal and vertical axis have units in degrees.

respectively and  $N_1$  &  $N_2$  are the relative strengths of each temperature component. We note that ESM spectra are collected for a shorter acquisition time and also have a jitter associated with the particle position with respect to the focal waist. In the x-ray spectrum, the low-intensity contributions are eliminated by the electronic triggering system and only high-intensity laser exposures are incorporated in the spectrum. The spectral differences if any are due to these features. The most important feature of high energy electron emission is identical in both measurements.

Electron emission is in the plane of laser polarization and figure 3 shows the measured angular distribution where we see two beams directed at about  $\pm 60^\circ$  to the laser propagation axis, opposite to the laser propagation direction. The laser polarization is rotated using half wave plate by  $0^\circ$  (S-polarization),  $45^\circ$  and  $90^\circ$  (P-polarization) and obtained electron angular distribution is shown in three panels of figure 3 respectively. The rotation of the plane of polarization rotates the electron emission plane and the twin electron beams have about  $2^\circ$  (FWHM) divergence (solid angle). Electron emission is critically dependent upon a deliberately introduced pre-pulse (a main pulse replica of 2%–5% in intensity which arrives about 4 ns ahead of the main pulse). Hot-electron production is boosted by 100-fold under otherwise identical conditions with the pre-pulse as illustrated in figure 2(a). Note that the ‘No pre-pulse’ data shown in figure 2(a) is still collected with a small fraction ( $\approx 1\%$ ) of pre-pulse, which is found to be essential to get any measurable high energy x-ray signal. Electron emission beyond 10 keV is completely eliminated without the pre-pulse ( $\approx 1\%$  of the main pulse) and typical laser pulse contrast here is  $10^{-5}$ . The electron charge measured per solid angle experimentally is about 220 pC/sr/s/MeV and the total charge per laser pulse is about 350 fC/shot/sr peaking at 200 keV.

#### 4. Numerical simulations

The microparticle orientation is random and measurements integrated over a large number of laser shots justify assumptions of modeling it as a  $15\ \mu\text{m}$  sphere. 2D PIC simulations [64, 65] with parameters (laser and the target) close to those employed in the experiments, give an electron temperature of at most 40 keV as shown in figure 4(a) (red spheres), which is consistent with the earlier scaling laws [26]. This is nearly an order of magnitude lower than the measurements in experiments. As seen in figure 2, the high-energy electron emission occurs only when there is a pre-pulse (2%–5% in intensity) arriving at about 4 ns ahead of

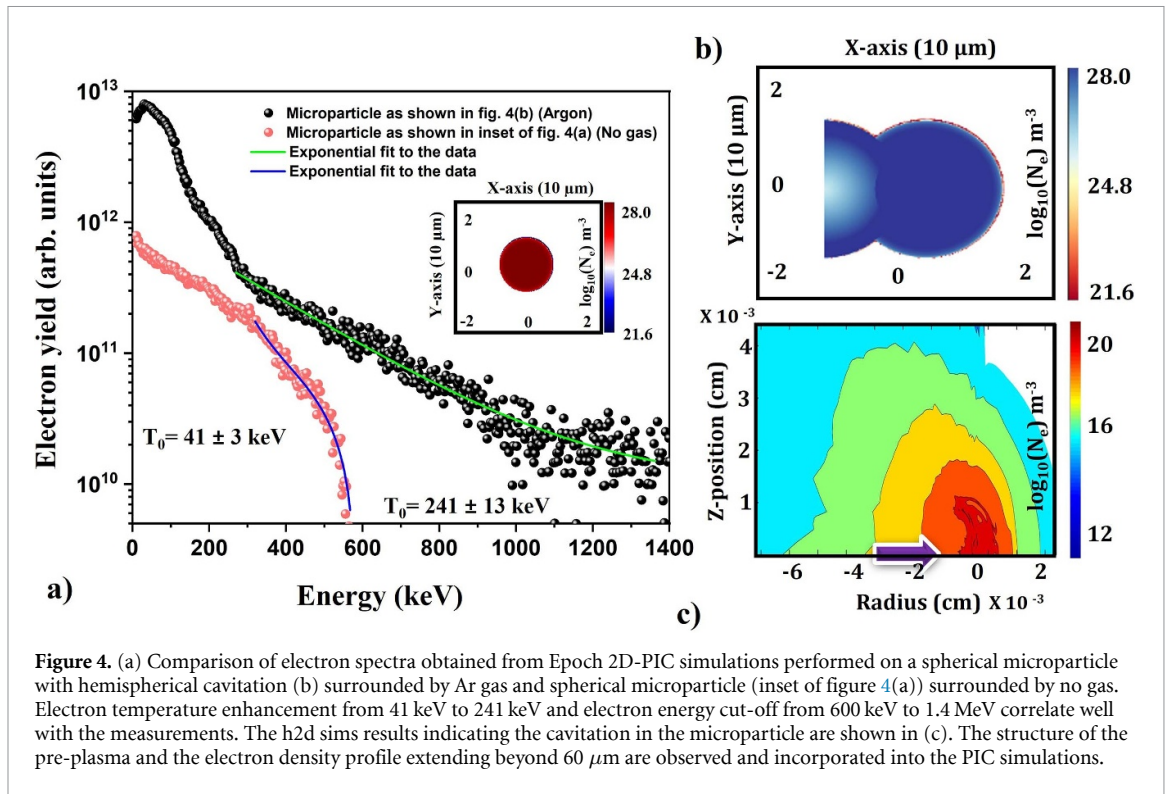


**Figure 4.** (a) Comparison of electron spectra obtained from Epoch 2D-PIC simulations performed on a spherical microparticle with hemispherical cavitation (b) surrounded by Ar gas and spherical microparticle (inset of figure 4(a)) surrounded by no gas. Electron temperature enhancement from 41 keV to 241 keV and electron energy cut-off from 600 keV to 1.4 MeV correlate well with the measurements. The h2d sims results indicating the cavitation in the microparticle are shown in (c). The structure of the pre-plasma and the electron density profile extending beyond 60  $\mu\text{m}$  are observed and incorporated into the PIC simulations.

the main pulse. The pre-pulse is expected to make changes in the pre-plasma conditions that would evolve and expand over 4 ns creating a relatively hotter pre-plasma. Simulations with different plasma-density scale lengths or other changes in initial plasma conditions did not yield a temperature close to that of the measurement. So, the pre-plasma evolution over nanosecond time scales was addressed using Lagrangian 2D-radiation hydrodynamics h2d code—Hyades. Hyades code [66, 67] simulates morphological changes in the target shape and also provides time evolution of pre-plasma temperature, electron density, etc.

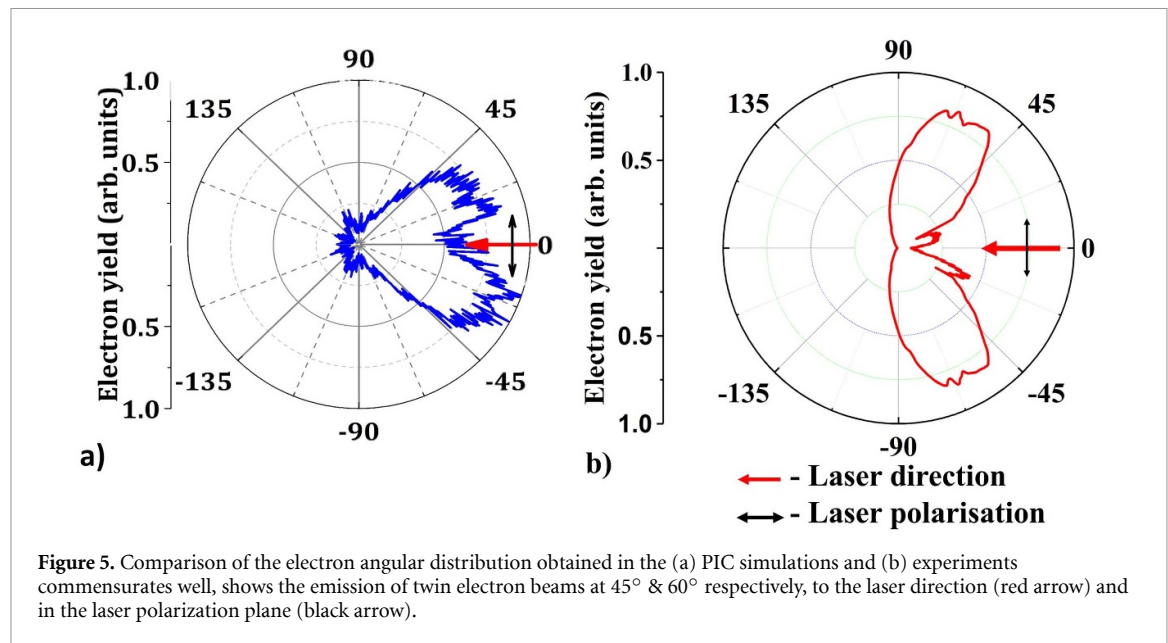
#### 4.1. Radiation hydro simulations

The h2d code simulations are run with an average atom local thermal equilibrium (LTE) ionization model and multigroup radiation diffusion. A 7.5  $\mu\text{m}$  spherical mesh of 0.792  $\text{g cm}^{-2}$  is exposed to 25 fs (FWHM), sech<sup>2</sup>, 800 nm pulse of 0.1 mJ energy to simulate pre-pulse interaction. A ray-tracing algorithm is used to mimic the focused 14  $\mu\text{m}$  FWHM Gaussian beam in the experiment. The final on-target intensity is  $0.2 \times 10^{16} \text{ W cm}^{-2}$ , 5% that of the main pulse. A cylindrical symmetry is assumed about the axis of laser incidence. The computed electron density, 4 ns after the pre-pulse interaction shows the formation of a large cup-shaped cavity as shown in figures 4(b) and (c) and so the main pulse energy is deposited in this cup-like hemispherical feature. Such cavity formation is also experimentally verified by shadowgraphy measurements that used a 15  $\mu\text{m}$  spherical liquid droplet target.

#### 4.2. 2D PIC simulations

To probe further we do 2D PIC simulations for two different targets. (i) A spherical particle of the size given in the inset of figure 4(a) and with the electron density,  $N_c$  (critical density). (ii) Inspired by the Hyades simulations, the pre-plasma structure is taken as shown in 4(b) with details as below. The electron acceleration results are compared by placing the target in the center of the simulation box. We use an  $80 \times 80 \mu\text{m}^2$  box size with  $3000 \times 3000$  cells filled with Ar gas of  $10^{17} \text{ atoms cm}^{-3}$  to closely mimic the experimental conditions. Ions are treated as a stationary background and there are 49 macro-particles per cell. The electron density is taken to be given by  $n_e/n_c = 7$  for  $r/\lambda_0 < 10$  and  $r_c/\lambda_0 > 13$ , and  $n_e/n_c = 7 \cos(\pi(r-10)/10)$  for  $r/\lambda_0 < 15$  and  $r_c/\lambda_0 > 13$ , where  $r_c = \sqrt{(x-30)^2 + (y-50)^2}$  is the radius measured to the cup center at  $x = 30\lambda_0$  and  $y = 50\lambda_0$ ; the cup electron density is given by  $n_e/n_c = 7 \exp(-(13-r_c)^2/4) + 0.01$  for  $x/\lambda_0 > 30$  and  $r_c/\lambda_0 < 13$ . A laser pulse of normalized vector potential  $a = a_0 \sin(\pi t/\tau)^2$  is launched from the left boundary, where  $a_0 = 0.2$  corresponds to a peak intensity of  $8.6 \times 10^{16} \text{ W cm}^{-2}$  and  $a_0 = 1$  to  $2 \times 10^{18} \text{ W cm}^{-2}$  with  $\tau = 25T_0 = 25\lambda_0/c$  is the duration 24.3 fs (FWHM in intensity profile) of the laser pulse. The laser is of Gaussian transverse profile and has a waist radius of  $W_0 = 12\lambda_0$ . The computational routines include field ionization of the gas to simulate the low-density plasma formed





surrounding the high-density microparticle. A virtual circular detector/screen surrounding the target is used to record the energy and angular distribution of the ejected electrons. The comparison of the electron energy spectrum obtained is shown in figure 4(a). It is observed that for  $a_0 = 0.2$  (intensity— $8.6 \times 10^{16} \text{ W cm}^{-2}$ ), the maximum electron energy is about 600 keV and the hot electron temperature is about 40 keV. Pre-plasma structure as shown in figure 4(b) results in two-hot electron temperatures (55 and 180 keV). It is thus understood from the simulations and experiment, that high electron energies are only possible when the pre-pulse distorts the spherical particle. Hot electron emission is thus enhanced and depends on the nature of distortion in the micro-particle shape.

Consistent with the experiments: (i) electron spectra fit a 41 keV and 241 keV temperature spectrum, commensurate with maximum electron energy. (ii) Electron angular distribution shows (figure 5(a)) twin beams on either side of the laser as measurements given in figures 3 and 5(b). The transient electric field evolution in time is extracted and the maximum of the magnitude of  $|E| \simeq \sqrt{E_y^2 + E_x^2}$  is obtained. The transient fields on the microparticle are of  $\simeq 0.1 \text{ TV m}^{-1}$  and the peak is about  $0.175 \text{ TV m}^{-1}$ . The pulse duration (FWHM) of the electron pulses of the energy range 10–1500 keV is obtained from the simulations and it is  $\leq 100 \text{ fs}$ , with 200–300 keV and 1.0–1.5 MeV energy electrons having  $43 \pm 2 \text{ fs}$  and  $5.3 \pm 0.2 \text{ fs}$  respectively. The experimental conditions would include deviations from the sphericity and symmetric distortions and could affect the results. A number of PIC simulations, with variations to incorporate the shape distortions and plasma scale length that might be expected, were performed. The absence of either the cavity or the low-density plasma gradient at the front surface eliminates the high-energy hot-electron generation even in the simulations.

## 5. Discussion

The necessity of the plasma gradient in the micro-cavity gives the first clue to understanding the role of the low-density plasma background. The low-density plasma gradient is formed by the background gas ionization. We further analyze PIC simulation results to understand the underlying mechanism of electron generation. The  $n_e$  and electric fields at different points of space and time are extracted and a Fourier analysis of the fields shows the generated plasma waves. The  $n_e$  and electric fields at different points of space and time are extracted and a Fourier analysis of the  $|E|^2$  shows the K-spectrum of the generated plasma waves. In figure 6(a), the laser K-vector ( $k_0$ ) is pointing in the X-direction, and the polarization is in the Y-direction. The plasma wave K-vector ( $k_e$ ) being in the plane of  $k_0$  (but angling backward) and laser polarization is one of the initial signatures of parametric instability. It is well understood that the backward propagating plasmon results in maximum growth rates. The pre-pulse provides an exponentially decaying electron density profile of  $L/\lambda \simeq 4$ . The intense main pulse that arrives 4 ns later ionizes the background gas and builds an electrostatic plasma wave. Around the  $n_{cr}/4$  layer, the electromagnetic field drives a two-plasmon parametric instability and the plasma wave grows efficiently. The wave amplitude increases non-linearly [68, 69]. Landau damping [70] and wave breaking [71] is effective at an oblique angle due to the concave  $n_{cr}$  layer.

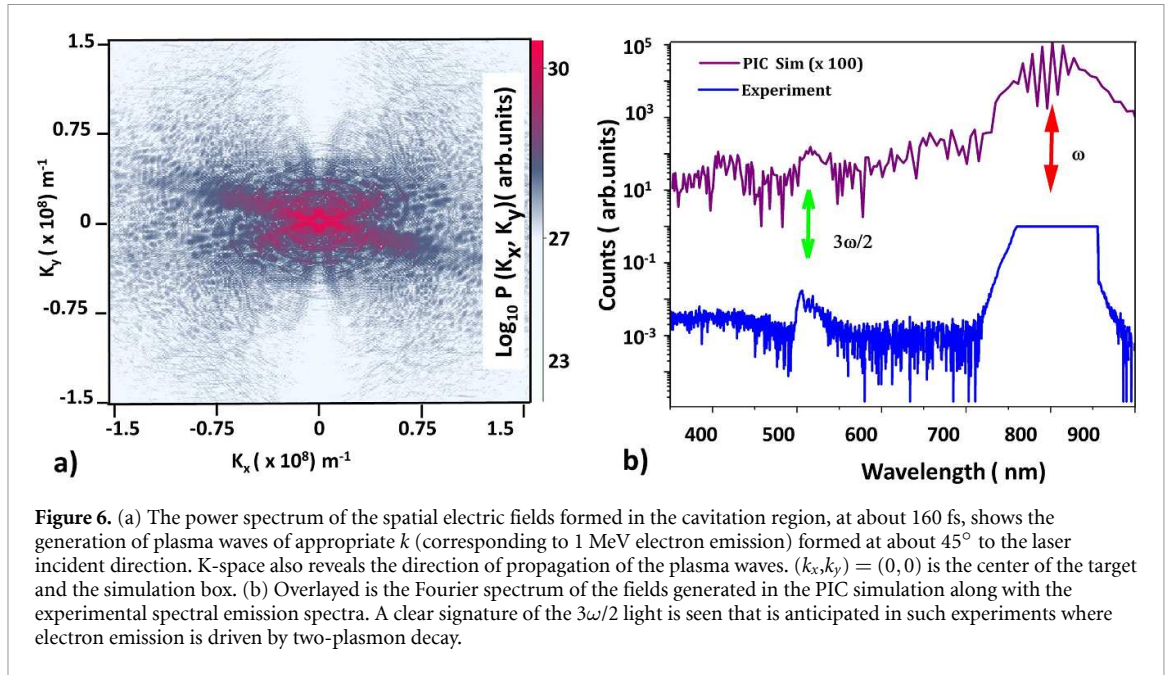


**Figure 6.** (a) The power spectrum of the spatial electric fields formed in the cavitation region, at about 160 fs, shows the generation of plasma waves of appropriate  $k$  (corresponding to 1 MeV electron emission) formed at about  $45^\circ$  to the laser incident direction. K-space also reveals the direction of propagation of the plasma waves.  $(k_x, k_y) = (0, 0)$  is the center of the target and the simulation box. (b) Overlaid is the Fourier spectrum of the fields generated in the PIC simulation along with the experimental spectral emission spectra. A clear signature of the  $3\omega/2$  light is seen that is anticipated in such experiments where electron emission is driven by two-plasmon decay.

A 2D  $k$ -spectrum of the plasma waves is obtained by performing spatial Fourier transform of an X-Y plot of the electric field at 160 fs and the plasma wave propagation seen in PIC (shown in figure 6(a)) gives a measure of the plasma waves emerging in the backward direction at an angle and with a  $k$ -value that correctly correlates with the measured  $k_B T_e$ . Calculating  $V_\phi \simeq \omega_p / \sqrt{(\gamma)k}$  and  $E_e \simeq (\gamma - 1)m_0 c^2$  for  $k = 0.04 \times 10^8/\text{m}$ , electron energy corresponds to 1.34 MeV, where  $V_\phi$  is the phase velocity of the wave,  $\omega_p$  is the plasma frequency,  $\gamma$  is the relativistic correction to the rest mass of the electron,  $k$  is the wave vector of the plasma wave. Thus the energy and the beam-like hot electron emission at about  $45^\circ$  and  $225^\circ$  in the plane of polarization seen in both experiments (figures 3 and 5) and simulations (figure 6) confirms the role of TPD. We note that the plane of emission of electrons in the form of twin beams has also been observed in PIC simulations [72]. The underlying effects of magnetic field generated in these systems are not possible with smaller laser intensities used in our experiments.

Fourier analysis of the plasma fields also shows the presence of  $3/2$  harmonic emission. These results prompted experimental observation of the  $3/2$  harmonic emission. The spectral measurement presented in figure 6(b) (blue curve) shows a clear signature of the  $3/2$  harmonic emission. As the pump pulse is shorter (30 fs) and has a larger bandwidth when compared to longer pulses, the  $3\omega_0/2$  harmonic emission is broader. Another reason for broader  $3\omega_0/2$  is that the  $T_e$  (keV) has a range in the order of a few keV due to a steeper gradient ( $L/\lambda = 4$ ). When compared with previous work [42], the  $\beta$  parameter for direct coupling for our experimental parameters is  $\ll 1$ , so the laser photons couples with  $\omega/2$  plasmons. Also, the pump laser intensity is much below the  $I_{th}$ . Thus we have direct proof of the TPD mechanism responsible for the hot electron generation. The following four points summarise the proof that the TPD mechanism is operational: (a) Electron energy larger than that possible with linear plasma resonance at these intensities, (b) Necessity of large low- $n_e$  plasma and the formation of exponentially decaying electron density profile, (c) Electron emission in the plane of laser polarization. (d) A direct measurement of  $3/2$  harmonic light emission from the target that correlates with hot electron emission.

The experiments and simulations presented here bring out several novel aspects of the well-studied TPD route for hot electron emission. (a) A mesoscopic particle suspended in low-density plasma effectively grows TPD instability. (b) Unlike, most earlier studies high energy pulses (Joule scale) and/or longer pulse durations which necessitate big lasers that operate at low repetition rates, mJ/pulse lasers with multi-kHz repetition rates are adequate. Such laser plasma studies are now accessible with moderate intensity femtosecond laser systems.

## 6. Summary

To summarise: experiments in which the microparticle is ionized to critical densities and the role of low-density background plasma is reported. The waves grow further along the density gradient of a concave critical density surface and yield hot electrons and x-rays with energies much larger than the conventional studies on a plain target. A laser pre-pulse modifies the microparticle target and forms a cavity, which

modifies the interaction with the main pulse dramatically. The hot electron temperature is about ten times larger than expected from a simple spherical or planar target. Twin electron beam emission tunable in the polarization plane is demonstrated. 2D PIC simulations explain both the experimentally observed electron emission and the role of the low-density plasma in electron temperature enhancement. Demonstration of the TPD instability with a 30 fs and 3 mJ laser pulse, is for the first time to the best of our knowledge. As the target morphology is modified and a pre-plasma of the concave cavity with an exponentially decaying electron density profile is formed, further deeper investigation (especially the wave growth and saturation of EPW) of the onset of TPD instability in such curved pre-plasma structures and mass-limited targets would be interesting.

This hitherto unexplored methodology has implications in engineering new sources with low energy, and high repetition rate lasers. This could prove useful from an applications standpoint and enable higher time-integrated yields by virtue of the significantly higher repetition rates available at such intensities.










## Data availability statement

The data that support the findings of this study are available upon request from the authors. All data that support the findings of this study are included within the article.

## Acknowledgments

M K thanks DST-SRC-OI grant. M K and V S thank the SPARC collaboration. D A E is thanked for the financial support to facilitate all the experiments. M K also thanks Prof. Robert Bingham for many insightful discussions.

## ORCID iDs

Rakesh Y Kumar  <https://orcid.org/0000-0002-7041-1759>  
 Ratul Sabui  <https://orcid.org/0000-0002-6999-8177>  
 R Gopal  <https://orcid.org/0000-0002-5776-9377>  
 William Trickey  <https://orcid.org/0000-0001-7013-4395>  
 John Pasley  <https://orcid.org/0000-0001-5832-8285>  
 R M G M Trines  <https://orcid.org/0000-0003-2553-0289>  
 A P L Robinson  <https://orcid.org/0000-0002-3967-7647>  
 V Sharma  <https://orcid.org/0000-0001-9830-2485>  
 M Krishnamurthy  <https://orcid.org/0000-0002-3442-1300>

## References

- [1] Mourou G and Umstadter D 1992 *Phys. Fluids B* **4** 2315
- [2] Joshi C *et al* 2007 *Phys. Plasmas* **14** 5
- [3] Albert F *et al* 2021 *New J. Phys.* **23** 031101
- [4] Joshi C *et al* 2020 *Phys. Plasmas* **27** 070602
- [5] Brunel F *et al* 1987 *Phys. Rev. Lett.* **59** 52
- [6] Wilks S C, Kruer W L, Tabak M and Langdon A B 1992 *Phys. Rev. Lett.* **69** 1383
- [7] Gibbon P and Bell A R 1992 *Phys. Rev. Lett.* **68** 1535
- [8] Gibbon P and Förster E 1996 *Plasma Phys. Control. Fusion* **38** 769
- [9] Parks G K, Lee E, Fu S Y, Lin N, Liu Y and Yang Z W 2017 *Rev. Mod. Plasma Phys.* **1** 1
- [10] Modena A *et al* 1995 *Nature* **377** 606
- [11] Malka V *et al* 2002 *Science* **298** 1596–600
- [12] Esarey E, Schroeder C B and Leemans W P 2009 *Rev. Mod. Phys.* **3** 1229
- [13] Marini S, Grech M, Kleij P S, Raynaud M and Riconda C 2023 *Phys. Rev. Res.* **5** 013115
- [14] Macchi A *et al* 2018 *Phys. Plasmas* **25** 3
- [15] Wen M, Salamin Y I and Keitel C H 2020 *Phys. Rev. Appl.* **13** 034001
- [16] Ramakrishna B *et al* 2010 *Phys. Rev. Lett.* **105** 135001
- [17] Rajeev P P, Taneja P, Ayyub P, Sandhu A S and Kumar G R 2003 *Phys. Rev. Lett.* **90** 115002
- [18] Fedeli L *et al* 2016 *Phys. Rev. Lett.* **116** 015001
- [19] Sarma J, McIlvenny A, Das N, Borghesi M and Macchi A 2022 *New J. Phys.* **24** 073023
- [20] Pukhov A, Sheng Z-M and Meyer-ter-Vehn J 1999 *Phys. Plasmas* **6** 2847
- [21] Arefiev A V, Robinson A P L and Khudik V N 2015 *J. Plasmas Phys.* **81** 475810404
- [22] Arefiev A V, Breizman B N, Schollmeier M and Khudik V N 2012 *Phys. Rev. Lett.* **108** 145004
- [23] Esarey E, Sprangle P and Krall J 1995 *Phys. Rev. E* **52** 5443
- [24] Thévenet M *et al* *Nat. Phys.* **12** 355 2016
- [25] Singh P K *et al* 2022 *Nat. Commun.* **13** 54
- [26] Kluge T, Cowan T, Debus A, Schramm U, Zeil K and Bussmann M 2011 *Phys. Rev. Lett.* **107** 205003
- [27] Meyer-ter-Vehn J and Sheng Z M 1999 *Phys. Plasmas* **6** 641

- [28] Paradkar B S, Krashenninnikov S I and Beg F N 2012 *Phys. Plasmas* **19** 060703
- [29] Robinson A P L, Arefiev A V and Neely D 2013 *Phys. Rev. Lett.* **111** 065002
- [30] Forslund D W, Kindel J M and Lindman E L 1973 *Phys. Rev. Lett.* **30** 739
- [31] Tabak M, Hammer J, Glinsky M E, Kruer W L, Wilks S C, Woodworth J, Campbell E M, Perry M D and Mason R J 1994 *Phys. Plasmas* **1** 1626
- [32] Boyd T J M et al 1986 *Plasma Phys. Control. Fusion* **28** 1887
- [33] Froula D H et al 2012 *Phys. Rev. Lett.* **108** 165003
- [34] Russell D A and DuBois D F 2001 *Phys. Rev. Lett.* **86** 428
- [35] Young P E, Lasinski B F, Kruer W L, Williams E A, Estabrook K G, Campbell E M, Drake R P and Baldis H A 1988 *Phys. Rev. Lett.* **61** 2766
- [36] Meyer J and Zhu Y 1993 *Phys. Rev. Lett.* **71** 2915
- [37] Baldis H A, Montgomery D S, Moody J D, Labaune C, Batha S H, Estabrook K G, Berger R L and Kruer W L 1992 *Plasma Phys. Control. Fusion* **34** 2077
- [38] Drake J F, Kaw P K, Lee Y C, Schmid G, Liu C S and Rosenbluth M N 1974 *Phys. Fluids* **17** 778
- [39] Turnbull D, Maximov A V, Edgell D H, Seka W, Follett R., Palastro J., Cao D, Goncharov V, Stoeckl C and Froula D 2020 *Phys. Rev. Lett.* **124** 185001
- [40] Yan R, Ren C, Li J, Maximov A V, Mori W B, Sheng Z-M and Tsung F S 2012 *Phys. Rev. Lett.* **108** 175002
- [41] Veisz L, Theobald W, Feurer T, Schillinger H, Gibbon P, Sauerbrey R and Jovanović M S 2002 *Phys. Plasmas* **9** 3197
- [42] Veisz L, Theobald W, Feurer T, Schwoerer H, Uschmann I, Renner O and Sauerbrey R 2004 *Phys. Plasmas* **11** 3311
- [43] Singh P K, Adak A and Lad A D 2015 *Phys. Plasmas* **22** 11
- [44] Singh P K, Adak A and Lad A D 2020 *Phys. Plasmas* **27** 083105
- [45] Tsymbalov I, Gorlova D and Savel'Ev A 2020 *Phys. Rev. E* **102** 0632206
- [46] Tarasevitch A, Dietrich C, Blome C, Sokolowski-Tinten K and Linde D von der 2003 *Phys. Rev. E* **68** 026410
- [47] Ivanov K A, Tsymbalov I N and Shulyapov S A 2017 *Phys. Plasmas* **24** 063109
- [48] Cowan T E et al 2004 *Phys. Rev. Lett.* **92** 204801
- [49] Palaniyappan S et al 2014 *Nat. Commun.* **6** 10170
- [50] Clerici M et al 2015 *Sci. Adv.* **1** e1400111
- [51] Shvedov V, Pivnev E, Davoyan A R, Krolikowski W and Miroshnichenko A E 2020 *Nat. Commun.* **11** 1
- [52] Zhang C, Huang C-K, Marsh K A, Clayton C E, Mori W B and Joshi C 2019 *Sci. Adv.* **5** eaax4545
- [53] Kozlova M et al 2020 *Phys. Rev. X* **10** 011061
- [54] Palmer C A J et al 2011 *Phys. Rev. Lett.* **106** 014801
- [55] Fukuda Y et al 2009 *Phys. Rev. Lett.* **103** 165002
- [56] Trivikram T M, Rajeev R, Rishad K P M, Jha J and Krishnamurthy M 2013 *Phys. Rev. Lett.* **111** 143401
- [57] Jha J et al 2008 *J. Phys. B: At. Mol. Opt. Phys.* **41** 041002
- [58] Levy D et al 2020 *New J. Phys.* **22** 103068
- [59] Augst S, Meyerhofer D D, Strickland D and Chin S L 1991 *J. Opt. Soc. Am. B* **8** 858
- [60] Gopal R, Kumar R, Anand M, Kulkarni A, Singh D P, Krishnan S R, Sharma V and Krishnamurthy M 2017 *Rev. Sci. Instrum.* **88** 023301
- [61] Rahul S V et al 2021 *AIP Adv.* **11** 015232
- [62] Tanaka K A, Yabuuchi T, Sato T, Kodama R, Kitagawa Y, Takahashi T, Ikeda T, Honda Y and Okuda S 2005 *Rev. Sci. Instrum.* **76** 013507
- [63] Anand M Kahaly S, Ravindra Kumar G, Krishnamurthy M, Sandhu A S and Gibbon P 2006 *Appl. Phys. Lett.* **88** 181111
- [64] Arber R T D et al 2015 *Plasma Phys. Control. Fusion* **57** 113001
- [65] Derouillat J et al 2018 *Comp. Phys. Commun.* **222** 351
- [66] Larsen J T and Lane S M 1994 *J. Quant. Spectrosc. Radiat. Transfer* **51** 179–86
- [67] H2d is a commercial product of Cascade Applied Sciences (available at: <https://casinc.com/h2d.html>)
- [68] Seka W, Edgell D H, Myatt J F, Maximov A V, Short R W, Goncharov V N and Baldis H A 2009 *Phys. Plasmas* **16** 052701
- [69] Wen H, Maximov A V, Short R W, Myatt J F, Yan R and Ren C 2016 *Phys. Plasmas* **23** 092713
- [70] Dawson J 1961 *Phys. Fluids* **4** 869
- [71] Katsouleas T and Mori W B 1988 *Phys. Rev. Lett.* **61** 90–93
- [72] Gong Z, Mackenroth F, Wang T, Yan X Q, Toncian T and Arefiev A V 2020 *Phys. Rev. E* **102** 013206